OPEN ACCESS

Engineered Catalyst Support with Improved Durability at Higher Weight Percentage of Platinum

To cite this article: Nagappan Ramaswamy *et al* 2023 *J. Electrochem. Soc.* **170** 114503

Journal of The Electrochemical Society, 2023 **170** 114503

Engineered Catalyst Support with Improved Durability at Higher Weight Percentage of Platinum

Nagappan Ramaswamy,[1,*,z] Barr Zulevi,[2,a] Geoff McCool,[2] Natalie Patton,[2] Zixiao Shi,[3] Aldo Chavez,[4] David A. Muller,[5,6] Anusorn Kongkanand,[1] and Swami Kumaraguru[1]

[1]*Global Fuel Cell Business, General Motors Company, Pontiac, Michigan 48340, United States of America*
[2]*Pajarito Powder, Albuquerque, New Mexico 87109, United States of America*
[3]*Department of Chemistry and Chemical Biology, Cornell University, Ithaca, New York, 14853, United States of America*
[4]*Department of Physics, Cornell University, Ithaca, New York 14853, United States of America*
[5]*School of Applied and Engineering Physics, Cornell University, Ithaca, New York 14853, United States of America*
[6]*Kavli Institute at Cornell for Nanoscale Science, Ithaca, New York 14853, United States of America*

Proton Exchange Membrane (PEM) fuel cells are a suitable electrochemical power source for heavy duty vehicle (HDV) applications due to their high efficiency and durability. The cathode of the fuel cell uses a higher geometric loading of platinum (~0.2 to 0.4 mg_{Pt}/cm^2) for the electrocatalysis of the kinetically sluggish Oxygen Reduction Reaction (ORR) which requires higher weight percent loading of the metal (~50%) on the carbon support to decrease the catalyst layer thickness and hence, the reactant transport losses. The conventionally used supports for platinum catalyst, such as the KetjenBlack™ type high surface area carbon (HSC) features limited mesopore area for the dispersion of Pt nanoparticles leading to increased aggregation and poor durability. Here, we show a new class of carbon materials known as the Engineered Catalyst Support (ECS) developed by Pajarito Powder with higher mesopore fraction for the dispersion of higher weight percentage of Pt nanoparticles. ECS materials can disperse up to 50% Pt by weight of the catalyst thereby enabling lower catalyst layer thickness with higher performance retained after durability test. A comprehensive set of physico-chemical and electrochemical studies in membrane electrode assembly (MEA) are reported to understand the performance and durability of Pt/ECS catalysts.
 [DOI: 10.1149/1945-7111/ad0668]

Manuscript submitted July 20, 2023; revised manuscript received October 12, 2023. Published November 2, 2023.

PEM fuel cells are a highly efficient, low-noise and zero-emission electrochemical power source for HDV applications and are widely considered as a replacement for the incumbent diesel-powered internal combustion engines.[1] The cathode of the fuel cell is a major source of both cost and performance loss as it uses a large amount of the expensive Pt catalyst, roughly 0.2 to 0.4 mg_{Pt}/cm^2, to conduct the kinetically sluggish four-electron transfer ORR.[2–5] The United States Department of Energy (DOE) has established an ultimate HDV performance and durability combined target of 2.5 kW/g_{Pt} after 30,000 h equivalent of operation (~equal to a million miles driving distance) with a total membrane electrode assembly (MEA) Pt loading of $\leqslant$0.25 mg_{Pt}/cm^2 for Class 8 long-haul tractor-trailers.[6]

Use of a high Pt geometric loading in the cathode catalyst layer (CCL) will require higher weight percent of Pt on the carbon support so that the catalyst layer thickness can be reduced, and the reactant (H^+/O_2) transport losses can be minimized.[7] The CCL thickness at a given geometric Pt loading is determined by the nature of the carbon support (particularly its bulk or packing density) and the weight percent of Pt on the carbon support. Typically, a CCL thickness of 10 ± 2 μm is considered optimal to enable lower reactant transport resistances and minimize flooding related issues.[8–10] KetjenBlack™ EC-300J type HSC support is a state-of-the-art cathode support, which at a weight percent of 30% Pt enables good, uniform dispersion of Pt nanoparticles.[11] HSC material feature internal surface area due to its micro- and meso-pore content thereby spatially separating Pt from the poisonous perfluorosulfonic acid (PFSA) ionomer side chains and along with its higher disordered content enables improved durability with less Pt nanoparticle aggregation.[12–15] At a particle size of ~3 nm diameter, the inter-particle distance is observed to decrease from 7.2 nm to 4.9 nm as the Pt weight loading on the HSC support increases from 20 to 40%.[16] However, as the Pt weight percent increases to 50% on the HSC support, Pt nanoparticles begin to deposit on the external surface of the carbon primary particle due its limited micro- and mesopore content accompanied by a decrease in interparticle distance and an increased aggregation of the nanoparticles.[13,16] One crucial feature of the carbon support to enable higher weight percent of Pt is to feature a higher mesopore fraction of the total surface area which aids in both Pt dispersion, reactant accessibility and durability.[15,17–20]

In this article, we describe and demonstrate a novel engineered carbon support developed by Pajarito Powder, LLC with a desired combination of characteristics, including higher mesoporosity for Pt dispersion, open hierarchical pore structure for improved reactant (H^+/O_2) accessibility, which result in better performance and durability in fuel cell MEAs. This carbon support is referred to as ECS3701 and achieved better initial performance at higher Pt weight percent of 50% due to better dispersion of Pt nanoparticles on the mesopore surface fraction. The electrochemical and physical properties of Pt/ECS3701 are compared to that of commercially available Pt/HSC catalyst at both 30% and 50% Pt weight percent. Pt/ECS3701 catalyst represents a significant improvement in performance and durability over the conventional porous carbon such as Pt/HSC at higher metal loading of 50% Pt and the results are discussed here in detail.

Experimental

Catalysts materials and MEA fabrication.—ECS3701, a commercially available carbon support, was produced by Pajarito Powder using their VariPore™ technology. The general ECS production method has been described in Refs. 21–25 which involves a mixture of a nitrogen-rich organic precursor, fumed silica, and any required metal precursor that is then pyrolyzed at high temperature. The silica template is removed with hydrofluoric acid, resulting in a carbon support with large amount of mesopore structure. This carbon support is washed, dried, and heat treated under a controlled atmosphere to generate ECS3701. Once ECS3701 is produced, platinum is then chemically deposited onto the surface pores of the engineered carbon support. The Pt/ECS3701 at a

*Electrochemical Society Member.
[a]Present address: Electric Hydrogen, Natick, Massachusetts 01760, USA.
[z]E-mail: nagappan.ramaswamy@gm.com

nominal metal loading of 30% and 50% Pt by weight of the catalyst are then washed, dried, and heat treated under a controlled atmosphere to ensure complete deposition. Pt supported on a KetjenBlack EC-300J (HSC) at nominal loadings of 30% and 50% Pt by weight of the carbon were also procured from Pajarito Powder. Cathode catalyst inks were made by dispersing the catalyst in n-propanol to water (3:1) solvent mixture with a PFSA ionomer featuring medium side chain length and an equivalent weight of 825 g mol^{-1}. The weight percentage of carbon in the catalyst with respect to the total catalyst ink weight was 3% and 5% for HSC and ECS3701 supported catalysts, respectively. Optimized ionomer to carbon ratios of 0.9 and 1.0 were used for Pt/HSC and Pt/ECS3701 catalysts, respectively. Cathode inks were coated on decal substrates at 0.20 mg_{Pt}/cm^2. All anode catalyst layers were composed of 20% Pt/C catalyst at a fixed loading of 0.050 mg_{Pt}/cm^2 and ionomer to carbon ratio of 0.6. MEAs with 5 cm^2 active area were fabricated via decal transfer of the anode and cathode catalyst layers on either side of a 12 μm thick, 800EW PFSA membrane in the H^+ form. Roughly 230 μm thick carbon fiber paper-based gas diffusion layer was used on both the anode and cathode side.

Physical characterizations of catalysts.—Analysis of the N_2-adsorption surface area and pore size distribution of the catalyst powders was carried out using a Micromeritics Instrument Corporation ASAP 2020 Physisorption system. N_2 gas of ultra-high purity was used, and the measurements were conducted at 77 K. Total specific surface area of the catalyst was determined using the Brunauer–Emmett–Teller (BET) procedure in the range of 0.05–0.2 N_2 partial pressure, pore-size distribution was quantified using Barrett–Joyner–Halenda (BJH) methodologies, and micropore surface area was quantified using the t-plot analysis.[19,26] Water uptake was measured volumetrically with a 3Flex Dynamic Vapor Sorption instrument at 25 °C. Characterization of the crystal structures and graphitic nature of the samples was performed using X-ray diffraction (XRD) on a Rigaku MiniFlex 600 (Rigaku Co., Japan) with monochromated Cu Kα radiation (λ = 1.5406 Å). Raman Spectroscopy was carried out using a Thermo DXR2 Raman spectrometer equipped with a 532 nm laser.

Electrochemical diagnostics and characterizations.—*In situ* characterizations of the MEA to quantify various cathode properties such as kinetic activity, H-adsorption ECSA, CO adsorption/stripping ECSA, H_2/air polarization curves, and H^+ and O_2 transport resistances were carried out in a single-cell test fixture comprising of 5 cm^2 active area MEA (0.5 mm lands/channels). Typically, six MEAs were tested for any given electrocatalyst providing sufficient reproducibility in test results. Prior to performance and durability measurements, MEAs were subjected to an extensive ~30 h break-in protocol that involved activation cycles and voltage recovery steps. The details of the break-in protocol are available elsewhere.[27] ECSA was quantified via integration of the hydrogen adsorption/desorption (H_{UPD}) region from cyclic voltammetry measurements of the cathode carried out at room temperature and 100% relative humidity (RH) conditions using H_2 and N_2 gas feeds on the anode and cathode sides at flow rate of 0.2/0.2 slpm, respectively. Oxygen reduction reaction (ORR) activities were measured at 0.9 V using the polarization curves obtained with pure H_2 and O_2 as the reactant gases in the anode and cathode, respectively at a stoic of 20. The RH of the inlet gas was maintained at 100% with the cell temperature maintained at 80 °C at an absolute outlet pressure of 150 kPa_{abs}. The activity at 0.9 V was determined using the Tafel plot, which is a semi-log plot of the Ohmic-resistance corrected cell voltage versus H_2 gas crossover corrected current density. H_2/air polarization curves with high stoichiometric feed of the reactant gases were measured at various operating conditions with cell temperatures ranging from 80 to 94 °C, RH values from 65 to 100%, and absolute outlet pressures of 150 to 250 kPa_{abs}. High-frequency resistance (HFR) to quantify the sum of cell electronic resistance and membrane H^+ transport resistance was measured at an alternating current (AC) frequency of 5 kHz.

A modified cathode catalyst-specific accelerated stress test (AST) recommended by the U.S. DOE was used in this study which consisted of 30,000 to 90,000 trapezoidal voltage cycles from 0.6 to 0.95 V. The dwell time at 0.95 V was 2 s and at 0.6 V was 1 s. A ramp time of 0.5 s was used in both directions. Each cycle took 4 s. AST durability protocols were carried out in 5 cm^2 MEAs with H_2/N_2 flow at 90 °C, 100% RH and ambient pressure.[28]

Proton transport resistance of the catalyst layer was measured using an electrochemical impedance spectra (EIS) methodology,[29] which involved the flow of H_2 on the anode and N_2 on the cathode at 80 °C and various RH values from 20% to 122%. EIS measurement was conducted to quantify proton conduction resistance at a DC potential of 0.2 V with 0.15 mV amplitude from a frequency of 0.5 Hz to 20 kHz with twenty points per decade. The EIS profile was fitted to a transmission line model from which the proton transport resistance in the membrane ($R_{H+,membrane}$) and the cathode ($R_{H+,cathode}$) were obtained. O_2 transport resistance was calculated using the limiting current density measurements at low O_2 partial pressures under operating conditions of 80 °C and 62% RH at differential cell conditions (1 slpm of H_2 and 5 slpm of O_2/N_2 mixtures).[30] O_2 limiting current densities were measured at potentials below 0.3 V at various O_2 mole fractions (1% to 4%) as a function of outlet pressures (110 to 300 kPa_{abs}). O_2 transport resistances are measured in units of seconds/cm (s/cm).

Electron microscopy.—The Scanning Transmission Electron Microscopy (STEM) experiment was performed using ThermoFisher Titan Themis Cryo S/TEM with a Field Emission Gun (X-FEG), monochromator and probe corrector operated at 120 kV and room temperature. The High-Annular angle dark field (HAADF) and Bright Field (BF) images were collected with 195 mm camera length and 21.4 mrad. convergence angle. The HAADF images were taken with 2048*2048 pixels and 2~5 us dwell time. The Pt nanoparticle size distribution were measured manually using the ImageJ software with 250~300 nm field of view HAADF image, where it typically contains 250–400 Pt nanoparticles. The aspect ratio of each nanoparticle was calculated with the manually measured length and width. A Zeiss Field Emission Scanning Electron Microscopy (FE-SEM) equipment with an in-lens detector was used to collect images of the carbon support.

Results and Discussion

The physico-chemical properties of the two carbon supports were investigated using a suite of *ex situ* characterization techniques such as i) SEM imaging of the carbon support to understand the carbon particle sizes and the nature of aggregation (Fig. 1, ii) BET-BJH to understand the pore size distribution and the fractions of micro-, meso- and macropores (Figs. 2 and 3), iii) Raman spectra, XRD, TEM and volumetric water uptake to understand the carbon disordered content, graphitization levels etc (Fig. 4). Table I shows a few selected properties of the carbon and the catalyst materials.

Figure 1 shows representative microscopic images of the HSC and ECS3701 carbon supports. HSC support features primary particles of ~20–30 nm in size fused together into multiple particles mostly in a linear fashion which are then extensively aggregated to form a connected structure.[13,16] In contrast, ECS3701 features a much larger primary particle of ~0.4 to 1.0 μm size which is a result of the templated synthesis process.[31] Pore openings of roughly a few nanometers in width appear on the surface of ECS3701 carbon support.

Figures 2a and 2b shows the N_2 adsorption isotherms, the pore size distribution of the carbon and the catalyst materials. The N_2 adsorption isotherm of HSC follows the typical Type II isotherm in that there is a steep rise at low partial pressures of $p/p^\circ < 0.05$ indicative of micropores followed by a characteristic hysteresis at $p/p^\circ \sim 0.5$ to 0.6 as well as saturation at $p/p^\circ > 0.95$ due to a rapid

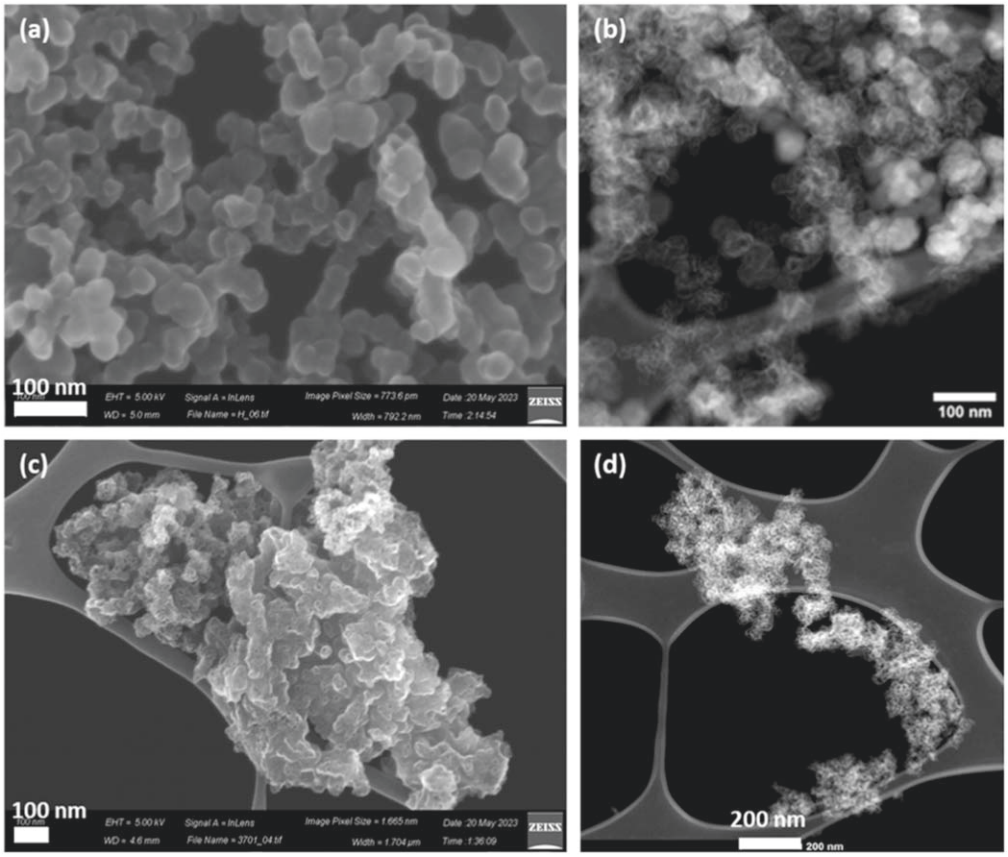

Figure 1. Secondary electron SEM images of a) HSC and c) ECS3701 carbon. Darkfield TEM images b) HSC and d) ECS3701.

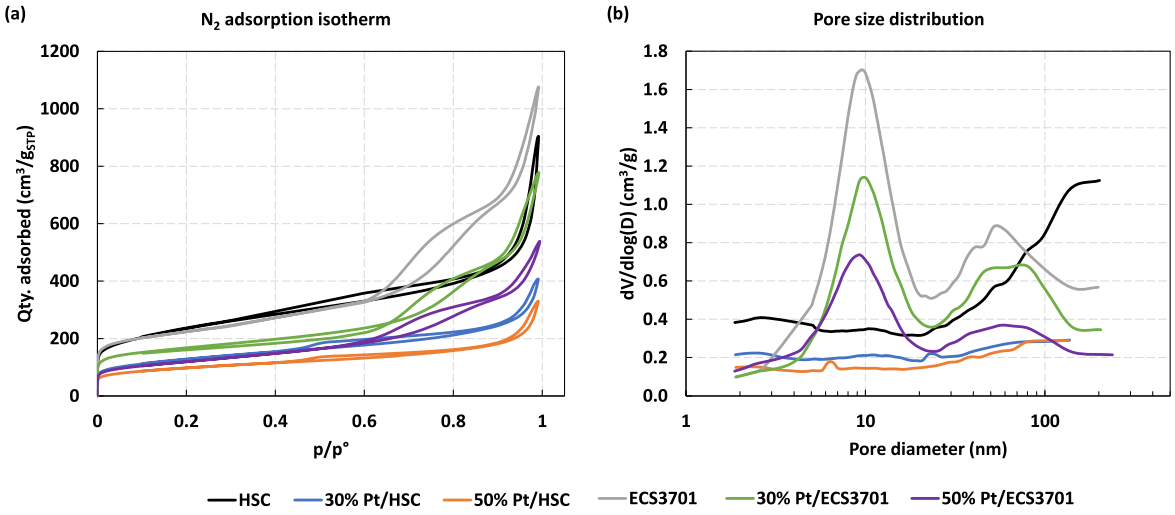

Figure 2. BET-BJH N_2 adsorption results showing the (a) isotherms and b) pore size distribution of the various carbon and catalyst materials.

uptake in the macropore region representative of aggregates.[19] The N_2 adsorption profile of ECS3701 is representative of a combination of Type II and Type IV in that it features a micropore region at $p/p^\circ < 0.05$, a change in slope at with increased N_2 uptake at $0.6 > p/p^\circ < 0.9$ indicative of ordering in mesopores, and finally a rapid uptake at $p/p^\circ > 0.90$ indicative of large aggregates.[32,33] With deposition of 30% and 50% Pt, the respective isotherms show a lower quantity of adsorption but with no major changes to the shape or profile of the isotherms.

Figure 2b shows the BJH adsorption pore size distribution from 2 to 200 nm region and Fig. 3 shows the division of the total surface area into micro-, meso- and macropores areas. The total BET surface area is also shown in Table I. Microporous surface areas were quantified from the t-plot method,[15,19,26] mesopore surface area was calculated from the cumulative area in the region 2 to 20 nm, and the macropore surface was calculated as the area above 20 nm in size. HSC support shows an almost unchanging surface area up to about 20 nm representing mesopores followed by a significantly higher macropore surface area above 20 nm. On the other hand, ECS3701 carbon appears to show two major peaks, one at ~9 nm mesopore region and another at ~50 nm macropore region. With the deposition of 30% and 50% Pt, the pore size distribution plots show a

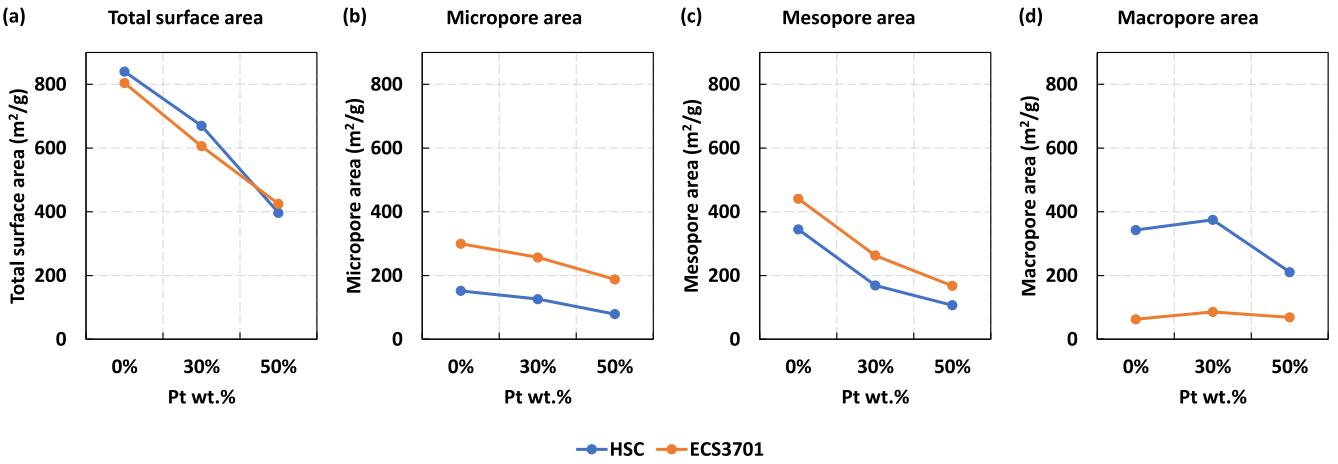

Figure 3. BET-BJH N_2 adsorption pore size results showing the (a) total BET surface area, (b) micropore area <2 nm, (c) mesopore area from 2 to 20 nm and (d) macropore area >20 nm.

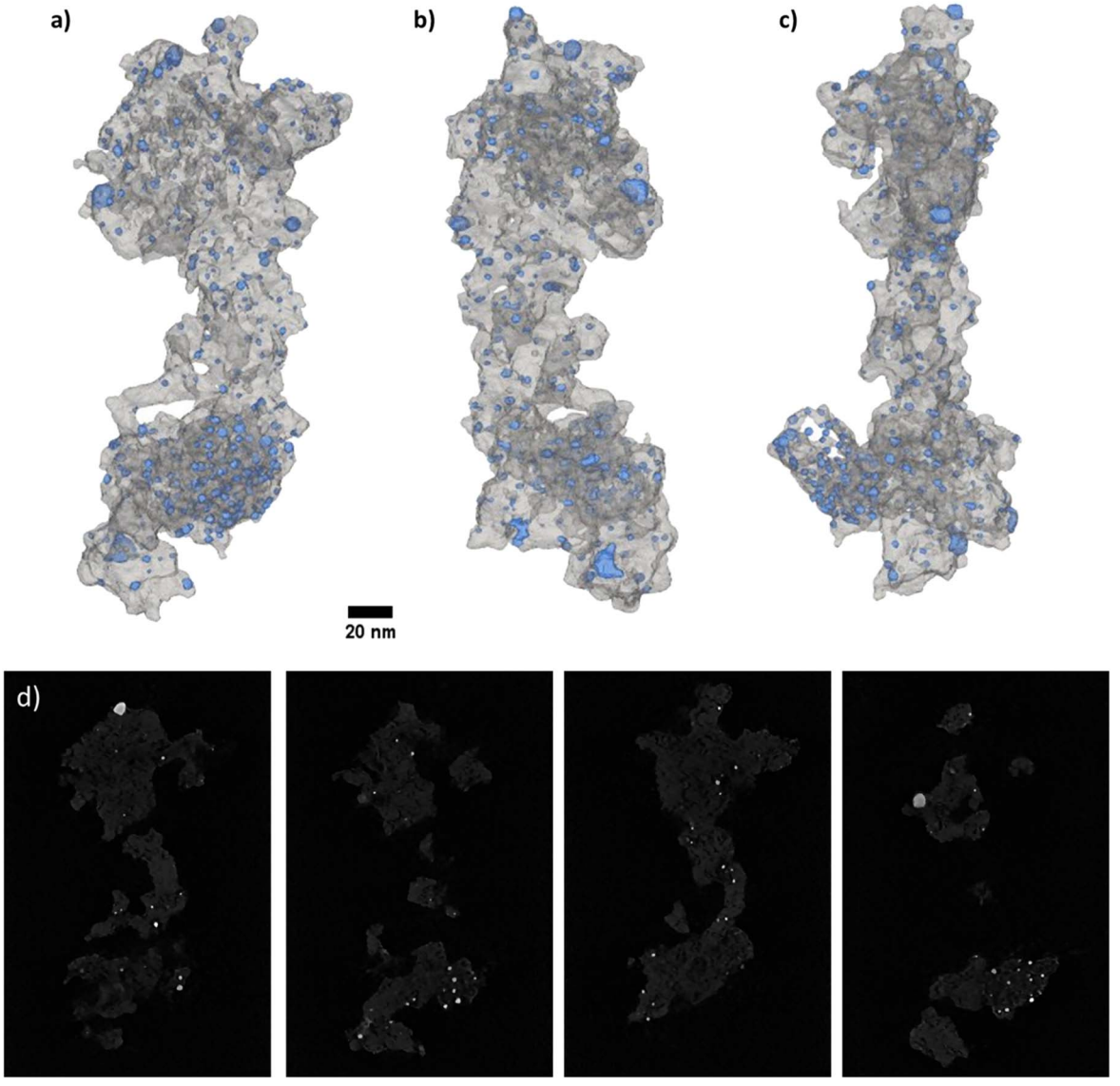

Figure 4. (a-c) TEM tomography images of 30% Pt/ECS3701 catalyst at three different rotation angles of −20°, +14°, +56°, (gray—carbon, blue—Pt nanoparticles) and (d) 2D cross-sectional slices of the tomography images.

Table I. Physico-chemical properties of the materials used in this study and the CCL thickness at 0.2 mg_{Pt}/cm^2 Pt loading.

					TEM BOL results		
Carbon/Catalyst	Pt wt%	I_D/I_G ratio	Pt XRD crystallite Size (nm)	BET surface area (m^2/g)	Mean Pt particle size (nm)	Aspect ratio	CCL thickness (μm)
HSC Carbon	n/a	1.19	n/a	840	n/a	n/a	n/a
30% Pt/HSC	28.5%	n/a	2.8	670	2.4	1.3	15.2 ± 0.9
50% Pt/HSC	46.9%	n/a	3.1	397	2.5	1.4	8.5 ± 0.8
ECS3701	n/a	1.01	n/a	804	n/a	n/a	n/a
30% Pt/ECS3701	27.1%	n/a	2.4	606	2.3	1.3	19.6 ± 0.4
50% Pt/ECS3701	46.0%	n/a	3.1	425	3.6	1.2	10.8 ± 0.6

respective drop in differential adsorption but with no major changes in pore size distribution. The plots in Fig. 3 capture the changes in surface areas more accurately as discussed below.

The total BET surface area of HSC and ECS3701 carbons are roughly similar at about 840 and 804 m^2/g but its distribution into the individual regions is substantially different. ECS3701 shows significant micro- and mesopore areas of 300 and 441 m^2/g but substantially lower macropore area of 63 m^2/g. HSC carbon shows lower micro- and mesopore area of 152 and 345 m^2/g but a substantially higher macropore area of 343 m^2/g. Upon 30% Pt deposition, both the carbon shows a significant decrease in mesopore area (∼40 to 50%) suggesting that Pt nanoparticles are likely deposited in the mesopore region of the carbon support. There is a marginal decrease in the micropore surface as well (∼15%). Upon further increase in deposition of Pt content to 50% by weight of carbon, there is decrease in both micropore (∼26%) and mesopore areas (∼36%) for ECS3701 material but the macropore area relatively remains constant. For HSC material, there is a drop in micropore and mesopore area of ∼37% each along with a significant drop in macropore area of ∼44%. This suggests that in increasing Pt weight percent from 30% to 50%, the additional Pt tends to get deposited on micropore and mesopore areas for both carbons but also on the external macropore area for the HSC support.[13] Even after 50% Pt catalyst deposition, the ECS3701 support still features a higher micro- and mesopore area available on its surface compared to HSC support.

Figures 4a–4d shows the STEM tomography images at different rotation angles and 2D cross-sectional slices of the 30% Pt/ECS3701. The Pt nanoparticles are largely deposited on the internal surface of the ECS3701 porous carbon support. While an attempt was made to separately color code the Pt nanoparticles on the internal versus the external surface, this proved to be difficult as most of the Pt particles were on the internal area with only a very small fraction on the external surface. The STEM tomography of Pt/HSC catalyst was reported previously,[13] wherein at 10% Pt vast majority of Pt nanoparticles were embedded in the internal surface. At 50% Pt weight percent on HSC, the formation of Pt nanoparticles on the external macropore surface became apparent.

Figure 5 shows the utilization or the location-distribution of Pt with respect to the pore structure of the carbon support measured via electrochemical CO_{ad} stripping surface areas as a function of inlet RH.[13,34] The electrochemical oxidation of CO_{ad} is reliant on access to water according to the equation $Pt\text{-}CO_{ad} + H_2O \rightarrow Pt + CO_2 + 2H^+ + 2e^-$ and hence is dependent on the RH of operation. Under a relatively dry condition of 20% RH, Pt nanoparticles present inside the micro-/meso-pores of the carbon particles are not accessed. Further, the Pt dry accessibility also depends on the continuity of the ionomer films dispersed on the carbon support, with more continuous ionomer films connecting more Pt ionically. Discontinuous ionomer films will require condensed water on the carbon catalyst to connect the ionomer patches.[15] Hence, the dry accessibility or utilization at 20% RH represents the fraction of Pt present on the external surface of the carbon in direct contact with the continuous layer of ionomer. All catalysts show an increase in Pt utilization with increasing RH, as expected, due to the condensation of water on the catalyst/ionomer surface thereby connecting ionomer regions and creating proton transport pathways.[35,36] On both the carbon supports, the Pt utilization at a dry condition of 20% RH is higher for 50% Pt than 30% Pt case. This suggests that the dry accessibility improves with increasing Pt weight percentages. For HSC support, the first 30% of Pt is largely deposited in the internal surface of carbon support, i.e., micro- and mesopore areas leading to a relatively lower utilization of ∼42% at 20% RH. Upon increase in Pt weight percent to 50%, the additional Pt is largely deposited on the external surface area, i.e., the macropore area, in direct contact with the ionomer leading to ∼71% utilization at 20% RH.

For ECS3701 carbon, the Pt utilization increase is quite significant as the Pt weight percent increases from 30% to 50% Pt. 30% Pt/ECS3701 shows a Pt dry accessibility of ∼20% whereas it increases to ∼80% for 50% Pt/ECS3701. The lower dry accessibility of 30% Pt/ECS3701 likely relates to the primary particle size and the pore structure of the ECS3701 carbon support. ECS3701 features large primary particles of up to ∼1 μm size with possibly deeper mesopores and discontinuous ionomer patches such that Pt deposited are not very accessible. Upon increase of Pt weight percent to 50%, the density of Pt nanoparticles increases inside the mesopores with shorter Pt-Pt interparticle distance and with the presence of Pt near the surface pore openings to improve its accessibility. Further at 50% Pt/ECS3701, the CCL thickness substantially decreases compared to 30% Pt/ECS3701 (19.6 to 10.8 μm, see Table I), and at 1.0

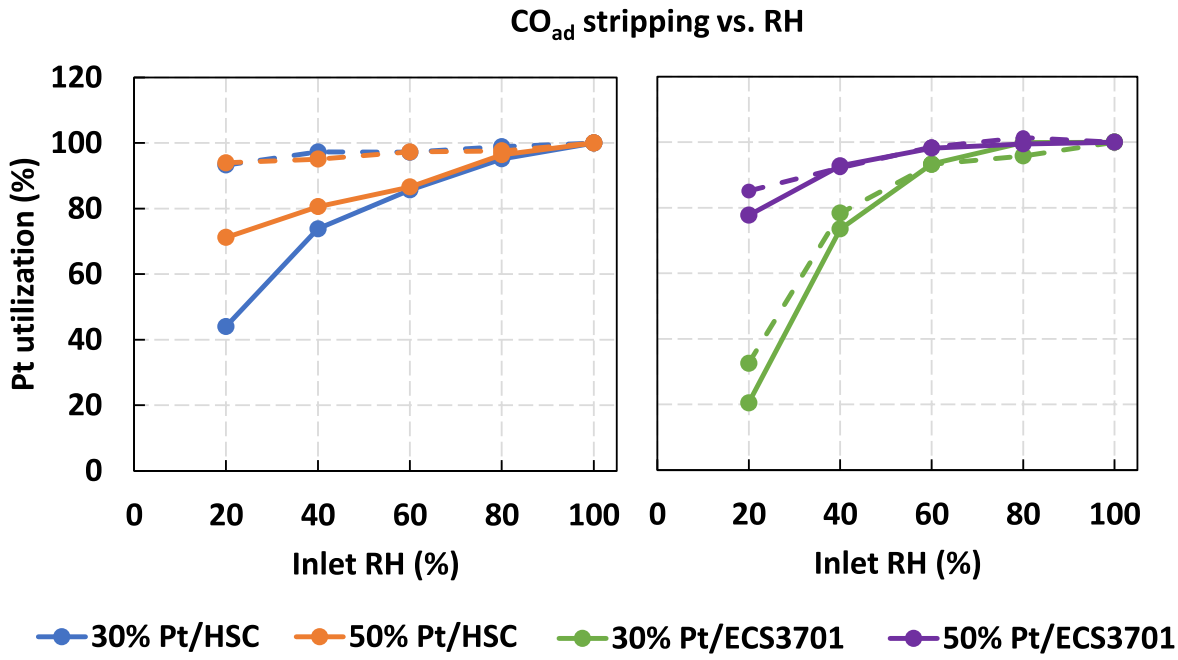

Figure 5. CO_{ad} stripping surface area measured as a function of the inlet RH in an MEA at 80 °C and 0.2 mg_{Pt}/cm^2. Solid lines are at BOL and dashed lines are at EOT after 30,000 voltage cycles.

I/C the ionomer has limited surface area of the carbon to disperse suggesting a more continuous ionomer layer thereby improving Pt accessibility.[15]

Figure 5 also shows the CO_{ad} stripping after 30,000 cycles of catalyst AST. Interestingly, for HSC support the Pt utilization improves significantly at both 30% and 50% Pt possibly due to the dissolution of Pt present in the internal surface of carbon support and its redeposition as Pt nanoparticles on the external surface thereby improving accessibility.[37] On the other hand, Pt/ECS3701 shows no major improvement in Pt accessibility at both 30% and 50% Pt. This is likely because the primary particle size of ECS (400–1000 nm) is much larger than HSC (20–30 nm), there is longer distance for dissolved Pt to diffuse and less external surface area to redeposit. As a result, small fraction of Pt redeposits on the external surface to change the accessibility after AST. As will be discussed below, microscopy analysis suggests increased level of particle migration-coalescence mechanism, which may partially contribute to the smaller change in ECS3701's accessibility after the AST test.

The level of disorder and the degree of graphitization of the carbons were investigated using Raman spectra and XRD patterns of the materials as shown in Figs. 6a and 6b. Raman spectra display two peaks at 1300 cm^{-1} and 1550 cm^{-1}, commonly known as the disorder (D) and graphitic (G) bands used to evaluate the relative trends in disorder through their ratio of intensities (I_D/I_G). ECS3701 support shows a lower disordered carbon content with I_D/I_G peak ratio of 1.01 compared to 1.19 for HSC support (Table I).[31] XRD profiles of the carbon supports show a similar profile with a broad peak at 23° and 43°, which are attributed to the (002) and (101) graphitic planes suggesting that the graphitic planes in these two carbons are of short-range order and are not crystallized.[38] Figure 6c and 6d shows the TEM images of KetjenBlack™ type HSC support and ECS3701 carbon support. HSC support is well known to feature turbostatic, disordered carbon content with a lack of graphitization.[39] ECS3701 carbon support shows a relatively more ordered graphitic surface planes but with short-range order (∼3 to 8 layers of graphene) around the mesopore regions. This suggests that the structural differences in the carbon support—while both are amorphous and non-graphitized structures ECS3701 is slightly more ordered than HSC support.

XRD patterns of 30% and 50% Pt/HSC and Pt/ECS3701 catalysts are also shown in Fig. 6e which reflects the peaks at 2θ values of 40°, 46°, 67° and 81° corresponding to the Pt diffraction peaks from (111), (200), (220), and (311) respectively confirming its face-centered cubic (fcc) structure.[40] In general, the XRD peaks for 50% Pt catalyst on any support is narrower than the 30% Pt indicating the larger Pt crystallite sizes at higher weight percent. The crystallite size of the Pt was also calculated using the Scherrer's equation from the full width at half maximum of Pt (220) diffraction peak and is reported in Table I. The Pt crystallite size increases from 2.4 nm to 3.1 nm for 30% and 50% Pt/ECS3701 catalysts respectively. On HSC support though, the Pt crystallites tend to be slightly larger with 2.8 nm and 4.1 nm at 30% and 50% Pt weight percent.

Volumetric water uptake at 25 °C on the two carbon supports is shown in Fig. 6f. Water adsorption on carbon supports could be divided into three regions: (i) water adsorption on surface functional groups in $0 > p/p^\circ < 0.4$, (ii) water adsorption and capillary condensation in primary pores in $0.4 > p/p^\circ < 0.9$ and (iii) water adsorption and capillary condensation in secondary pores at $p/p^\circ > 0.9$.[41] Figure 6f suggests that water uptake on ECS3701 carbon has an earlier onset and adsorbs water at relatively lower water partial pressure. On HSC support, water uptake does not occur until p/p° of 0.4 and shows substantial water uptake at $p/p^\circ > 0.6$. This suggests the presence of functional groups capable of water adsorption on ECS3701 carbon and the occurrence of capillary condensation in the primary pores. HSC features a delayed onset and capillary condensation in primary pores only at higher partial pressures of greater than 0.6.

Figure 7 shows the through-plane, bulk H^+ transport resistance of the CCL as a function of inlet RH with and without the thickness normalization for the four different catalysts. The $R(H^+)$-cathode decreases with increasing RH as expected and tends to plateau at higher RH values as more humidification of the ionomer phase in the electrode and water condensation on carbon surface aids in proton conduction. For any given carbon support, higher weight percent catalyst features a lower $R(H^+)$-cathode due to lower thickness of the CCL. However, both the catalysts deposited on ECS3701 carbon support shows a higher $R(H^+)$-cathode than the HSC support at all RH values. This is clearly observed in Fig. 7b after normalizing by the CCL thickness indicating that the proton transport resistance through the catalyst layer is dependent on the nature of the carbon support.[15] While this dependence is not completely understood, we hypothesize that the larger primary particle with lower macropore surface areas of the ECS3701 to be at least partially responsible for the higher H^+ transport resistance. The ionomer in the catalyst layer tends to be dispersed on the macropore surface area of the carbon support.[15] HSC with reasonable macropore area tends to disperse the PFSA ionomer throughout the CCL relatively in a more homogeneous fashion. ECS3701 support likely disperses the ionomer in a more aggregated and heterogenous fashion on the carbon support in the CCL leading to formation of patchy and discontinuous ionomer film. Despite this difference dependent on the nature of the support, higher weight percent catalyst enables lower $R(H^+)$-cathode on any given carbon support. For instance, at a CCL loading of 0.2 mg_{Pt}/cm^2, $R(H^+)$-cathode of 30% Pt/ECS3701 at 95% RH is 0.16 Ω cm^2 which decreases to 0.07 Ω cm^2 for 50% Pt/ECS3701. This difference of 0.09 Ω cm^2 corresponds to an *effective* H^+ transport resistance value in the CCL of 0.03 Ω cm^2. This yields an improved cell voltage by ∼75 mV at 2.5 A cm^{-2} for 50% Pt/ECS3701 clearly minimizing transport related voltage losses at high current densities compared to 30% Pt/ECS3701. Further, the higher through-plane H^+ transport resistance likely affects the current density distribution and hence, the catalyst utilization in the thickness direction of the catalyst layer with more utilization near the cathode/membrane interface and less utilization near the membrane/gas diffusion layer interface.[42]

Figure 8 shows a plot of the O_2 transport resistance measured from the limiting current density measurements. It can be divided into the pressure-dependent (not shown) and the pressure-independent O_2 transport resistances. Pressure-dependent transport resistance arises due to the molecular diffusion of O_2 in the cathode flow-fields and the large pores of the cathode gas diffusion layer (GDL) substrate. Given that the flow-fields and the GDL substrates are similar in these experiments, any differences between the O_2 transport resistance can be attributed to arise from the CCL. Pressure-independent transport resistance largely arises due to the i) Knudsen diffusion of O_2 in the small pores (<10 nm) of the microporous layer of the cathode GDL and the CCL, ii) diffusion of O_2 in the thin ionomer layer of the CCL. Pressure independent transport resistance is a strong function of the cathode Pt surface area and increases with decreasing ECSA. At BOL, the pressure-independent transport resistance of the catalysts on ECS3701 support is lower than the HSC support largely due to the open, mesopore structure of the ECS3701 carbon support that enables improved accessibility of O_2 to the Pt nanoparticles.[17] The pressure-independent transport resistance for each catalyst increases at EOT compared to its BOL due to the decrease in the surface area of Pt of all the catalysts.[43] On HSC support, it increases significantly at EOT for 50% Pt/HSC catalyst. On the contrary, it is the lowest for the 50% Pt/ECS3701 at EOT at 0.21 s cm^{-1}.

Figure 9 shows a boxplot of cathode ECSA, specific and mass activities at BOL and EOT after 30,000 catalyst AST cycles. All parameters in Fig. 9 drop in value from BOL to EOT whereas the specific activity alone increases in value after EOT (shown as hashed bars). Figure 10 shows the H_2/air polarization curves for all the catalysts at BOL and at EOT after running 30,000 voltage cycles of catalyst AST durability protocol. For Pt catalysts, the cell voltage in the kinetic region is largely determined by its mass activities whereas the high-current density performance is determined by a

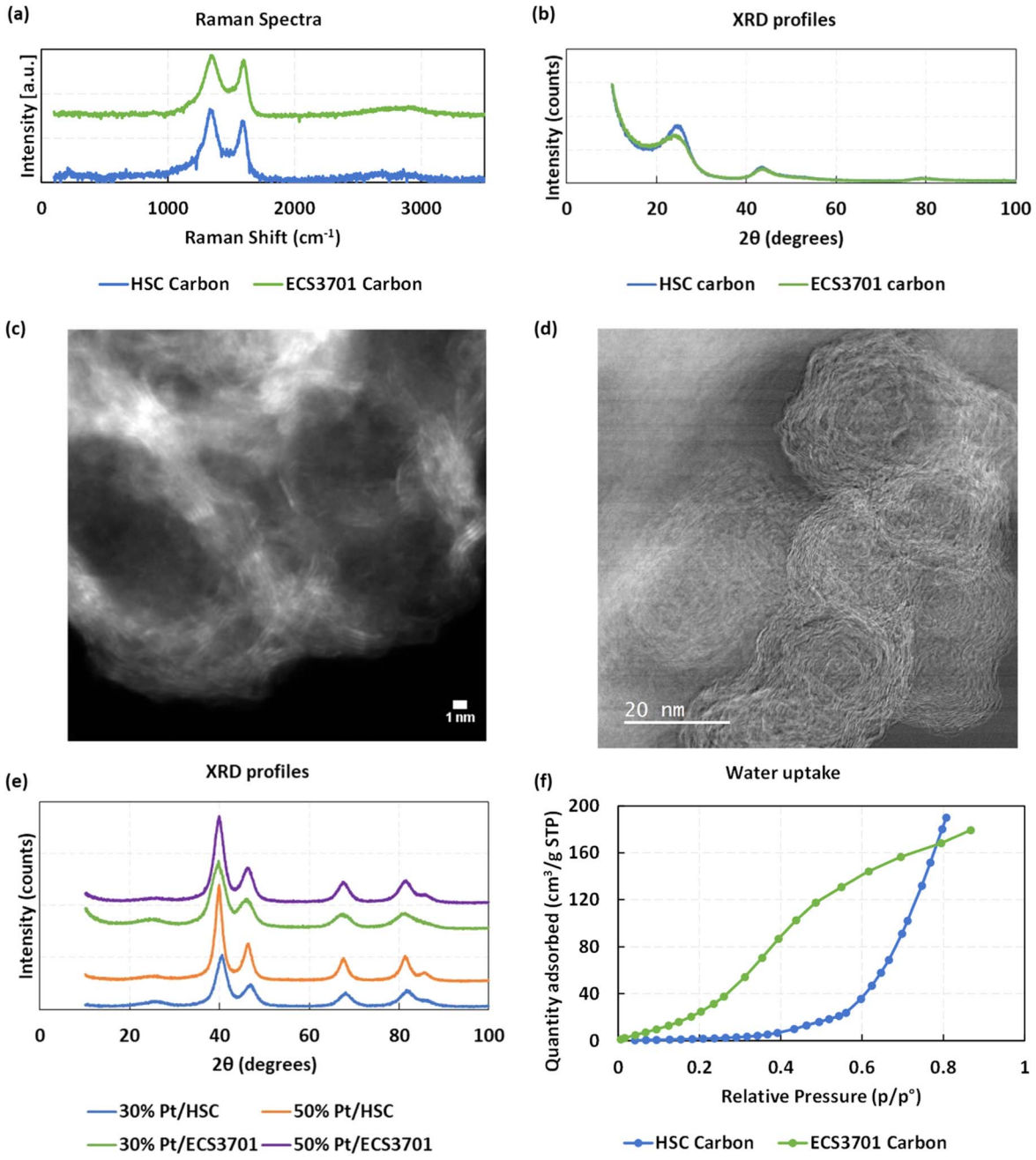

Figure 6. (a) Raman spectra, (b) XRD profiles of the carbon supports, TEM images of (c) ECS3701 and (d) HSC supports, (e) XRD profiles of the catalyst materials, and (f) volumetric water uptake of carbon supports at 25 °C.

combination of ECSA and transport factors. At BOL, the ECSA of 30% Pt/HSC is higher at ~69 m^2/g compared to 50% Pt/HSC at 50 m^2/g due to the larger Pt particle size for the latter. The mass activity at BOL of 30% Pt/HSC (0.38 A/mg_{Pt}) is higher due to Pt being deposited in the internal pores of the carbon support thereby being less poisoned by ionomer compared to 50% Pt/HSC (0.32 A/mg_{Pt}).[11,15,17] The specific activity at BOL of 50% Pt/HSC (639 $\mu A/cm^2_{Pt}$) is higher than 30% Pt/HSC ($\mu A/cm^2_{Pt}$) at least in part due to lower ECSA for the former compared to the latter. For HSC support at BOL, the kinetic region of the polarization curve shows that the 30% Pt is marginally better than the 50% Pt by ~10 mV at 0.2 A cm^{-2} as reflected in the mass activity values. The 50% Pt/HSC improves slightly in cell voltage at higher current densities and shows roughly similar cell voltages to 30% Pt/HSC mostly due to the thinner CCL enabling lower $R(H^+)$-cathode related transport losses. The CCL thickness of 50% Pt/HSC at 0.2 mg_{Pt}/cm^2 is 8.5 ± 0.8 μm versus 15.2 ± 0.8 μm for the 30% Pt/HSC at the same loading (Table I). At EOT, both the 30% Pt/HSC and 50% Pt/HSC catalysts loses ~25 mV in the kinetic region reflecting similar losses in mass activity of ~45% thereby maintaining the same separation of ~10 mV in cell voltage at 0.2 A cm^{-2}. At a high current density of 2.5 A cm^{-2} the cell voltage of 50% Pt/HSC shows a larger loss ~50 mV compared to 30% Pt/HSC. This is due to slightly lower surface area of 25 m^2/g and much higher pressure independent O_2 transport resistance for 50% Pt/HSC compared to 30% Pt/HSC catalyst at EOT. In general, for the HSC support the 30% Pt catalyst is more durable in cell voltage than the 50% Pt.

Interestingly for the ECS3701 carbon support, the 50% Pt/ECS3701 catalyst shows significant improvement in cell voltage at both BOL and EOT compared to 30% Pt/ECS3701. The ECSA values at BOL of 30% and 50% Pt/ECS3701 catalysts are 74 m^2/g and 59 m^2/g, respectively. These values are higher than the

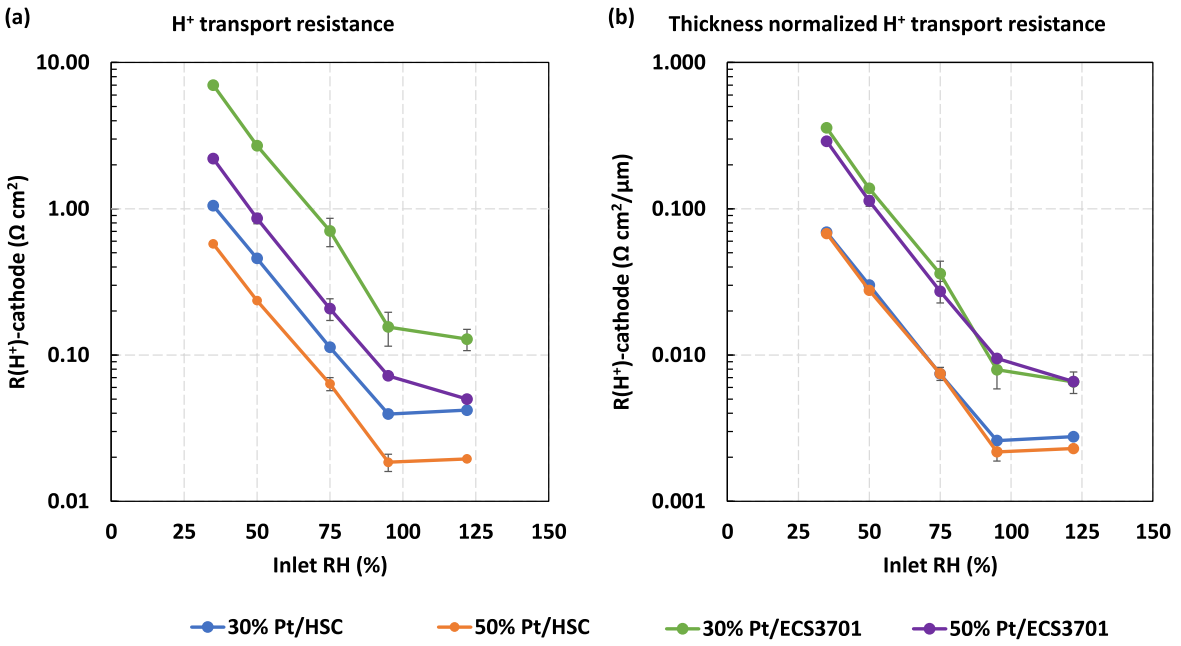

Figure 7. (a) Electrode H^+ transport resistance and (b) CCL thickness normalized electrode H^+ transport resistance measured from electrochemical impedance spectroscopy measured with anode/cathode flows of H_2/N_2 at 80 °C as a function of RH. CCL loadings were 0.2 mg_{Pt}/cm^2.

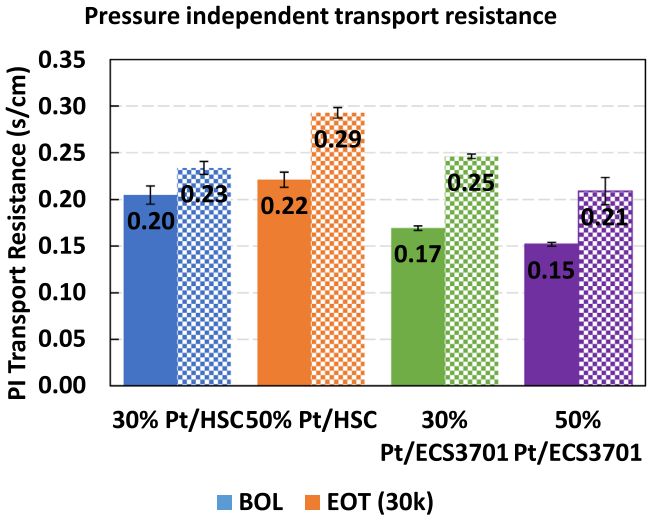

Figure 8. Results from the O_2-limiting current density measurements showing pressure independent resistance. Solid bars are at BOL and hashed bars are at EOT after 30,000 voltage cycles. O_2 transport resistance is represented in units of seconds/cm (s/cm).

corresponding HSC catalysts largely due to smaller Pt nanoparticle sizes achieved on ECS3701 carbon support at a given Pt weight percent. At BOL the 50% Pt/ECS3701 shows ∼15 to 20 mV improvement in the kinetic region (<0.2 A cm^{-2}) compared to 30% Pt/ECS3701 as reflected in the higher mass activity value of 0.48 versus 0.40 A/mg_{Pt}. It is interesting to note that for HSC support, the mass activity drops in value for the 50% Pt compared to the 30% Pt catalyst, whereas it improved for the ECS3701 carbon support. This is due to the Pt being deposited on the external macropore surface area of HSC support, thereby being poisoned due to direct contact with the ionomer functional groups. On ECS3701 support, the additional Pt particles at 50% Pt continues to deposit on the internal micro- and mesopore surfaces thereby not being poisoned by ionomer. At BOL, specific activity of 50% Pt/ECS3701 is also significantly higher at 873 μA cm^{-2} compared to 548 μA/cm^2 for 30% Pt/ECS3701. This is partly due to i) lower ECSA of 50% Pt/ECS3701 catalyst compared to 30% Pt/ECS3701, ii) lack of poisoning from the sulfonate groups and iii) better through-plane catalyst utilization of 50% Pt/ECS3701 given its lower thickness than the 30% Pt/ECS3701 (19.6 to 10.8 μm, see Table I). The lower H^+ transport resistance of 50% Pt/ECS3701 catalyst layer at its lower thickness compared to 30% Pt/ECS3701 (Fig. 7a) leads to better and more uniform catalyst utilization in the through-plane direction of the catalyst layer.

At BOL high current density of 2.5 A cm^{-2}, the cell voltage of 50% Pt/ECS3701 is clearly higher by ∼50 mV than 30% Pt/ECS3701. This is largely due to the lower through-plane H^+ transport resistance at lower CCL thickness and lower pressure independent O_2 transport resistance for 50% Pt/ECS3701 catalyst. At EOT, the ECSA values of the 30% and 50% Pt/ECS3701 decrease to similar value of ∼27 to 29 m^2/g but the percent loss is lower for 50% Pt/ECS3701 catalyst. 30% Pt/ECS3701 loses ∼61% of its original ECSA as opposed to ∼54% loss for the 50% Pt/ECS3701 catalyst. The cell voltage at 0.2 A cm^{-2} decreases by ∼20 mV for both 30% and 50% Pt/ECS3701 as reflected by the ∼50% loss in mass activity for both these catalysts. However, the 50% Pt/ECS3701 catalyst maintains a marginally higher cell voltage by ∼5 mV as reflected in its higher mass activity value at EOT. Further, the cell voltage at EOT at 2.5 A cm^{-2} is significantly better by ∼150 mV for 50% Pt/ECS3701 compared to 30% Pt/ECS3701 partly due to lower pressure independent O_2 transport resistance for 50% Pt/ECS3701 at EOT.

Figure 11 shows the cell voltage at 2.0 A cm^{-2} for all the catalysts as a function the number of AST cycles up to 90,000 voltage cycles. On HSC support, the 30% Pt catalyst is more durable than the 50% Pt after 90,000 cycles. This plot clearly shows the improved durability of the 50% Pt/ECS3701 compared to both the 30% Pt/ECS3701 and the HSC supported catalysts. 50% Pt/ECS3701 maintains a higher cell voltage of ∼500 mV at 2.0 A cm^{-2} after 90,000 AST cycles which is ∼60 mV better than the next best catalyst which is 30% Pt/HSC and ∼110 mV better than 50% Pt/HSC.

Figure 12 shows the HR-TEM images of the catalysts at BOL and at EOT after 30,000 AST cycles, and Fig. 13 shows the particle size distribution (PSD) of the Pt nanoparticles and their aspect ratios. While 30% Pt/HSC catalyst is finely dispersed into spherical Pt nanoparticles with a smaller average particle size of 2.4 nm, 50% Pt/

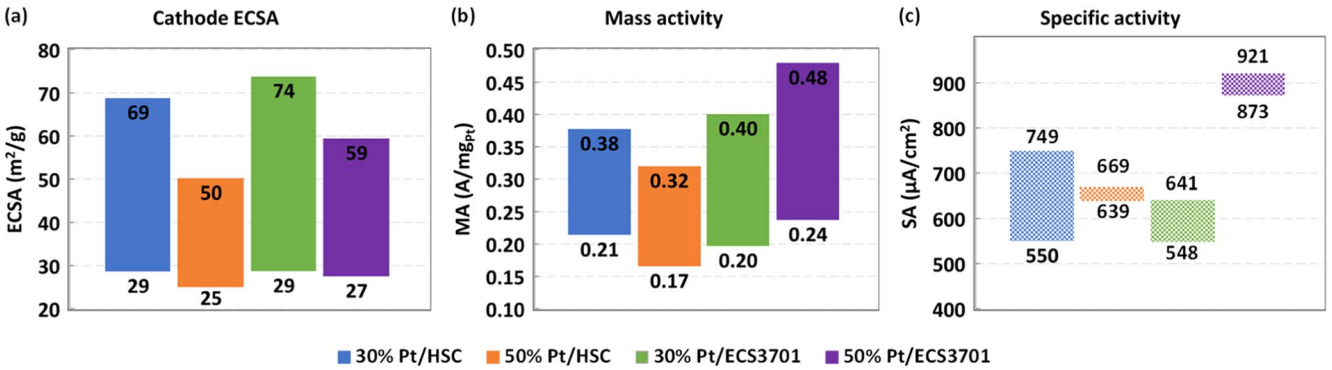

Figure 9. Boxplot showing the electrochemical characteristics of the catalysts showing (a) ECSA, (b) mass activity and (c) specific activity at BOL and at EOT after 30,000 AST cycles at 0.2 mg_{Pt}/cm^2 CCL loading. All parameters drop in value at EOT except for specific activity which increases in value at EOT (shown as hashed boxes). Error levels are within 3 to 10% of the average ECSA values, and within 5 to 13% of the average mass or specific activity values.

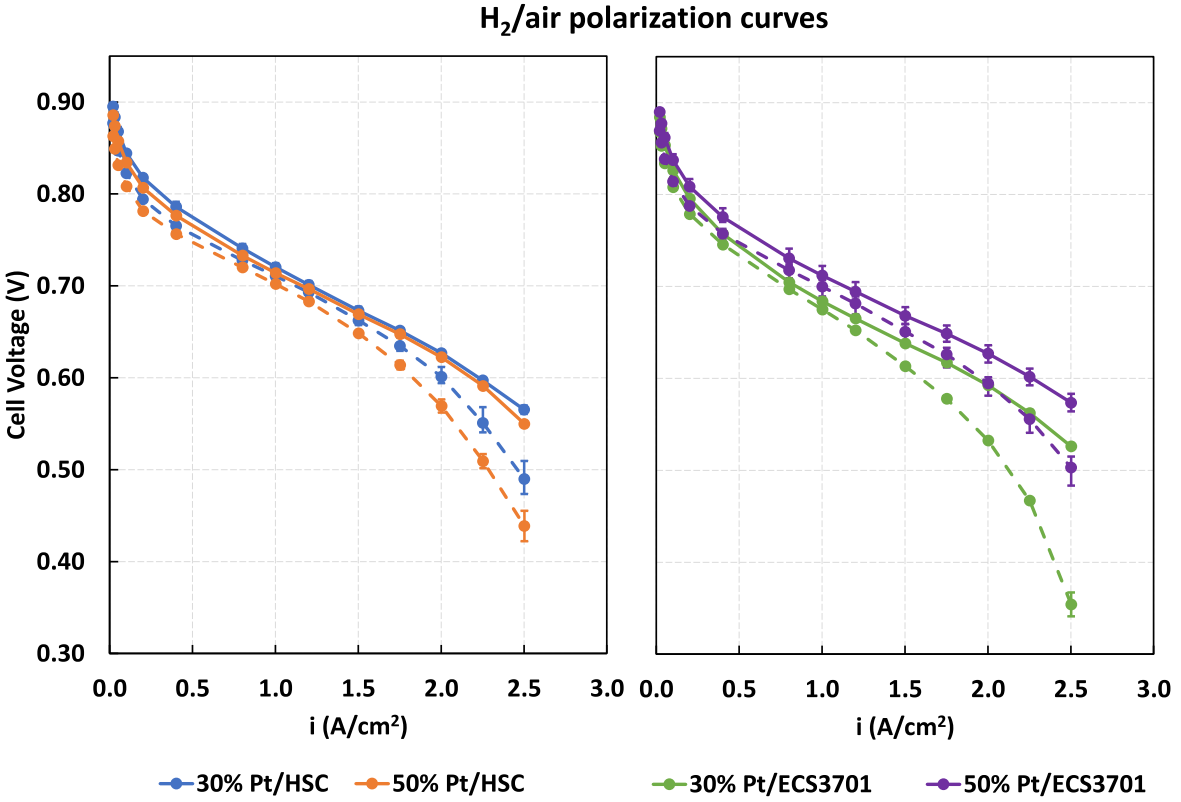

Figure 10. H_2/air polarization curves measured at 80 °C, 100% RH, 150 kPaabs, at a high stoic of 20 and at 0.2 mg_{Pt}/cm^2 cathode of the four catalysts. Solid lines are at BOL and dashed lines are at EOT after 30,000 voltage cycles.

HSC shows the presence of aggregated, and elongated Pt nanoparticles at BOL. This is likely due to the lower mesopore fraction of the surface area available for Pt dispersion on HSC support thereby leading to aggregation at a higher Pt weight percent of 50%. At EOT, the 30% Pt/HSC largely appears to maintain Pt nanoparticle sphericity suggesting that dissolution-redeposition of Pt (Ostwald ripening) is the dominant mechanism of particle coarsening. On the other hand, Pt nanoparticles tend to coarsen via migration-coalescence and form elongated nanoparticle structures for the 50% Pt/HSC catalyst as observed from the longer tail in the PSD and aspect ratio.[12] There is likely a transition in dominant particle ripening mechanism from Ostwald ripening at 30% Pt/HSC to the migration-coalescence phenomena at 50% Pt/HSC for the HSC support.

On ECS3701 carbon support at BOL, the Pt nanoparticles maintain their spherical shape with an aspect ratio of close ~1.2 to 1.3 at both 30% and 50% Pt weight percent with average particle sizes of 2.3 and 3.6 nm, respectively, although the catalyst is more densely populated with large particles for 50% Pt/ECS3701. Nevertheless, the higher mesopore fraction of ECS3701 enables a better dispersion of nanoparticles at 50% Pt weight percentage than HSC support. On the contrary, at EOT both 30% and 50% Pt/ECS3701 catalysts appear to coarsen via migration-coalescence as seen by the formation of fused and elongated Pt nanoparticles on the carbon support. At EOT, the mean aspect ratio for the Pt nanoparticles on ECS3701 at 30% and 50% weight percent are 1.6 and 2.0 compared to 1.3 and 1.7 for the catalyst on HSC support. We attribute this feature to the slightly higher degree of ordering in the carbon planes for ECS3701 support and the larger primary particles in the support featuring a more continuous internal surface. Pt dispersed on graphitized support with higher degree of ordering in

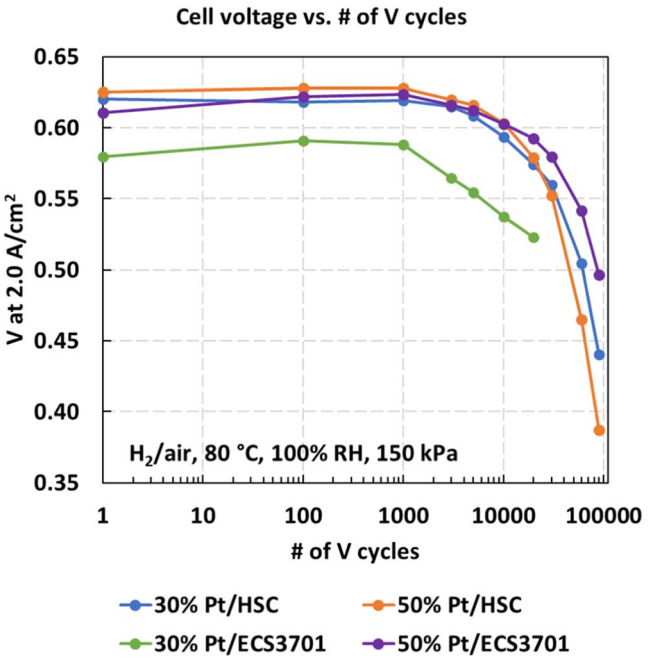

Figure 11. Cell voltage at 2.0 A cm^{-2} as a function of AST voltage cycles.

the carbon planes have previously been shown to coarsen via migration-coalescence with the formation of elongated particles as the dominant mechanism.[12,14]

In summary, we have demonstrated an alternative carbon support that provided better fuel cell performance retention. The ECS3701 possess large amount of mesopore with tighter size control giving less pressure independent oxygen transport resistance and less ORR kinetic penalty from ionomer adsorption. The large amount of mesopore allows for high level of Pt to be loaded into the carbon interior without significant oxygen transport loss or accelerated Pt degradation due to close interparticle distance. While its electrode proton transport resistance was 3–4 times higher than HSC, the overall fuel cell performance under a normal moderately wet operating condition did not suffer as much because the lower oxygen transport resistance and ORR kinetic penalty overcome the shortfall in proton resistance. TEM and Raman analyses suggested the higher degree of ordering in the carbon planes of ECS3701 led to formation of elongated particles after AST test via migration-calescence mechanism. Despite that, ECS3701 showed comparable, if not better, ECSA and ORR activity retention after AST test when compared to HSC catalysts. This is attributable to its larger, more ordered mesopore structure and its larger aggregate size.

As for next steps, clearly, further electrode optimization to lower the electrode proton resistance is a priority. Understanding the carbon surface chemistry may be necessary to form good ink and coating, as water uptake test showed significantly different water uptake profile. Smaller catalyst aggregate size (than the current 0.4–1 μm) may help. As the higher degree of ordering in the carbon planes may contribute to Pt coarsening, particle anchoring strategies such as N-doping or metal oxide adatoms can be promising.[7,44]

Conclusions

KetjenBlack^{TM} EC-300J type HSC support and an engineered carbon support from Pajarito Powder, namely the ECS3701, were compared in their properties to disperse Pt nanoparticles at two different weight percentages of 30% and 50%. Due to its higher mesopore fraction of the total surface area, ECS3701 support was able to better disperse a higher weight percent of 50% Pt nanoparticles at BOL with an aspect ratio representative of spherical particles. 50% Pt/ECS3701 catalyst also showed a significant improvement in cathode performance and durability after 90,000 cycles of AST compared to both 30% and 50% Pt/HSC. 50% Pt/ECS3701 maintained a higher cell voltage of ~500 mV at 2.0 A cm^{-2} after 90,000 AST cycles which is ~60 mV better than 30% Pt/HSC and ~110 mV better than 50% Pt/HSC. This is due to a combination of lower pressure independent O_2 transport resistance and higher ORR activity due to the presence of mesopores ECS3701. Development of ECS3701 carbon represents a significant step in enabling alternative catalyst support materials with an open, mesoporous structure for Pt dispersion at higher catalyst weight percent for HDV fuel cell applications.

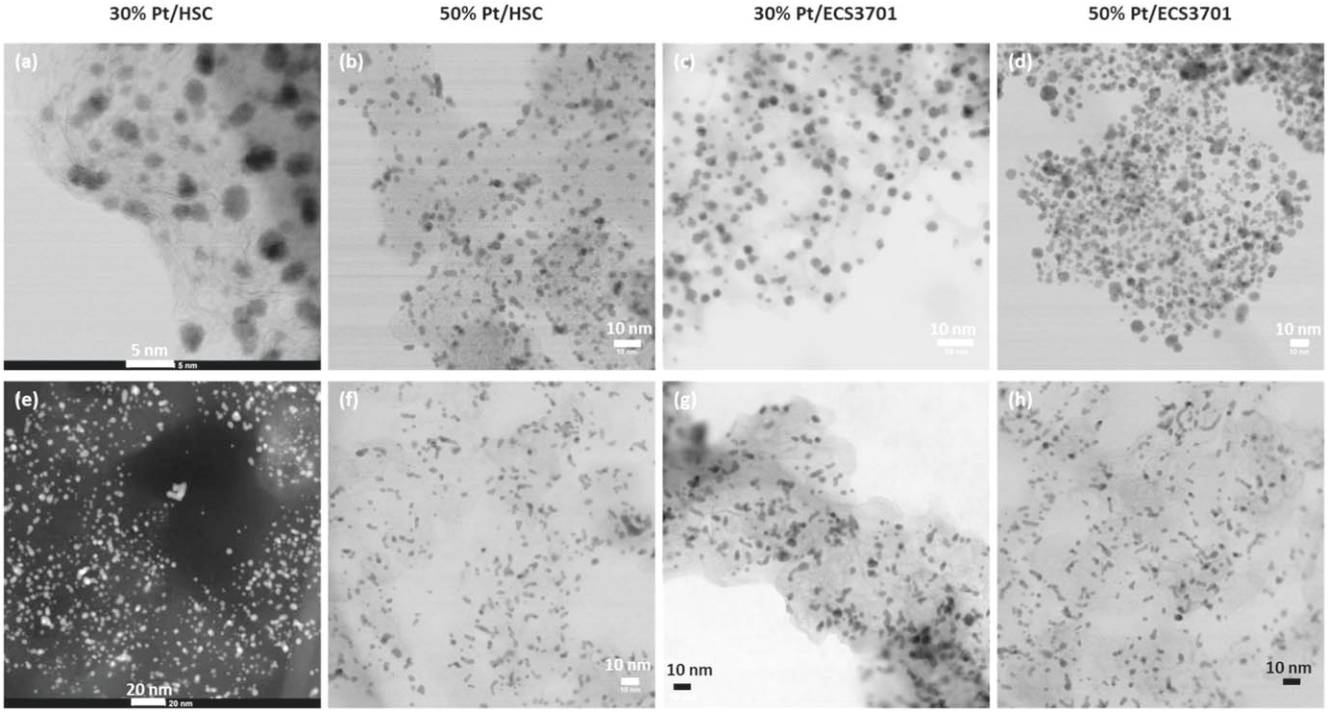

Figure 12. HR-TEM images of the catalysts at (a-d) BOL and (e-h) at EOT after 30,000 AST cycles.

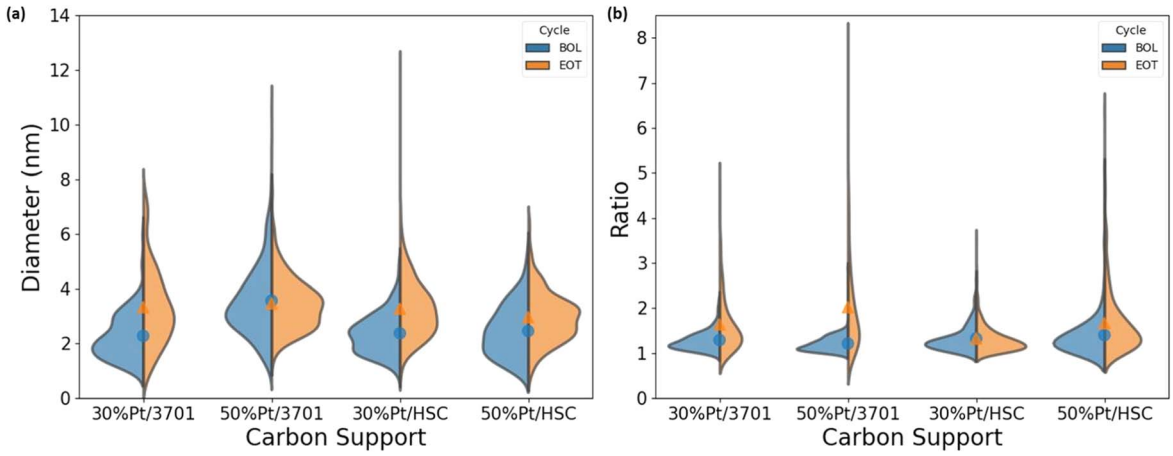

Figure 13. Violin plots showing the a) particle size distribution and b) aspect ratio of the Pt nanoparticles at BOL and EOT. Blue circular dot represents the mean value of BOL samples, and the orange triangular symbol represents the mean value of the EOT samples.

Acknowledgments

This work was partially supported by U.S. Department of Energy, Hydrogen and Fuel Cell Technologies Office under grant DE-EE0008821. Electron microscopy facility support from the Cornell Center for Materials Research under NSF Grant DMR-1719875 is acknowledged. The authors would like to acknowledge Kenneth Holt, David Ceu, Melanie Molotky, Kathryn Stevick and April Vaughter of GM for manufacturing and engineering support.

ORCID

Nagappan Ramaswamy https://orcid.org/0000-0002-3430-2758
Anusorn Kongkanand https://orcid.org/0000-0001-9250-3112
Swami Kumaraguru https://orcid.org/0000-0002-8644-2074

References

1. D. A. Cullen, K. C. Neyerlin, R. K. Ahluwalia, R. Mukundan, K. L. More, R. L. Borup, A. Z. Weber, D. J. Myers, and A. Kusoglu, "New roads and challenges for fuel cells in heavy-duty transportation." *Nat. Energy*, **6**, 462 (2021).
2. A. Kongkanand and M. F. Mathias, "The priority and challenge of high-power performance of low-platinum proton-exchange membrane fuel cells." *J. Phys. Chem. Lett.*, **7**, 1127 (2016).
3. Y. Sun, S. Polani, F. Luo, S. Ott, P. Strasser, and F. Dionigi, "Advancements in cathode catalyst and cathode layer design for proton exchange membrane fuel cells." *Nat. Commun.*, **12**, 5984 (2021).
4. C. S. Gittleman, A. Kongkanand, D. Masten, and W. Gu, "Materials research and development focus areas for low cost automotive proton-exchange membrane fuel cells." *Curr. Opin. Electrochem.*, **18**, 81 (2019).
5. H. A. Gasteiger, S. S. Kocha, B. Sompalli, and F. T. Wagner, "Activity benchmarks and requirements for Pt, Pt-alloy, and non-Pt oxygen reduction catalysts for PEMFCs." *Appl. Catal. B*, **56**, 9 (2005).
6. Million Mille Fuel Cell Truck Consortium. Available from: https://millionmile-fuelcelltruck.org/..
7. M. Chen, C. Li, B. Zhang, Y. Zeng, S. Karakalos, S. Hwang, J. Xie, and G. Wu, "High-platinum-content catalysts on atomically dispersed and nitrogen coordinated single manganese site carbons for heavy-duty fuel cells." *J. Electrochem. Soc.*, **169**, 034510 (2022).
8. I. V. Zenyuk, P. K. Das, and A. Z. Weber, "Understanding impacts of catalyst-layer thickness on fuel-cell performance via mathematical modeling." *J. Electrochem. Soc.*, **163**, F691 (2016).
9. P. K. Mohanta, M. S. Ripa, F. Regnet, and L. Jörissen, "Impact of membrane types and catalyst layers composition on performance of polymer electrolyte membrane fuel cells." *ChemistryOpen*, **9**, 607 (2020).
10. P. K. Das, X. Li, and Z.-S. Liu, "Analytical approach to polymer electrolyte membrane fuel cell performance and optimization." *J. Electroanal. Chem.*, **604**, 72 (2007).
11. S. S. Kocha, J. W. Zack, S. M. Alia, K. C. Neyerlin, and B. S. Pivovar, "Influence of ink composition on the electrochemical properties of Pt/C electrocatalysts." *ECS Trans.*, **50**, 1475 (2013).
12. E. Padgett et al., "Mitigation of PEM fuel cell catalyst degradation with porous carbon supports." *J. Electrochem. Soc.*, **166**, F198 (2019).
13. E. Padgett et al., "Editors' choice—connecting fuel cell catalyst nanostructure and accessibility using quantitative Cryo-STEM tomography." *J. Electrochem. Soc.*, **165**, F173 (2018).
14. X. Tuaev, S. Rudi, and P. Strasser, "The impact of the morphology of the carbon support on the activity and stability of nanoparticle fuel cell catalysts." *Catal. Sci. Technol.*, **6**, 8276 (2016).
15. N. Ramaswamy, W. Gu, J. M. Ziegelbauer, and S. Kumaraguru, "Carbon support microstructure impact on high current density transport resistances in PEMFC cathode." *J. Electrochem. Soc.*, **167**, 064515 (2020).
16. B. T. Sneed, D. A. Cullen, K. S. Reeves, O. E. Dyck, D. A. Langlois, R. Mukundan, R. L. Borup, and K. L. More, "3D analysis of fuel cell electrocatalyst degradation on alternate carbon supports." *ACS Appl. Mater. Interfaces*, **9**, 29839 (2017).
17. V. Yarlagadda, M. K. Carpenter, T. E. Moylan, R. S. Kukreja, R. Koestner, W. Gu, L. Thompson, and A. Kongkanand, "Boosting fuel cell performance with accessible carbon mesopores." *ACS Energy Lett.*, **3**, 618 (2018).
18. E. Antolini, "Carbon supports for low-temperature fuel cell catalysts." *Appl. Catal. B*, **88**, 1 (2009).
19. T. Soboleva, X. Zhao, K. Malek, Z. Xie, T. Navessin, and S. Holdcroft, "On the Micro-, Meso-, and macroporous structures of polymer electrolyte membrane fuel cell catalyst layers." *ACS Appl. Mater. Interfaces*, **2**, 375 (2010).
20. Y. Kamitaka, T. Takeshita, and Y. Morimoto, "MgO-templated mesoporous carbon as a catalyst support for polymer electrolyte fuel cells." *Catalysts*, **8**, 230 (2018).
21. A. Serov and P. Atanassov, "Carbendazim-based catalytic materials." *US Patent.*, 9,425,464 (2016).
22. A. Serov, B. Halevi, M. Robson, W. Patterson, K. Artyushkova, and P. B. Atanassov, "Cathode catalysts for fuel cell application derived from polymer precursors." *US Patent*, 9,502,719 (2016).
23. A. Serov and P. Atanassov, "Materials with atomically dispersed chemical moieties." *US Patent.*, 10,619,256 (2020).
24. A. Serov and P. B. Atanassov, "Non-PGM catalysts for ORR based on charge transfer organic complexes." *US Patent.*, 9,722,256 (2017).
25. A. Serov, P. B. Atanassov, B. Halevi, and P. Short, "Non-PGM catalyst for ORR based on pyrolysed poly-complexes." *US Patent*, 9,570,761 (2017).
26. S. Lowell, J. E. Shields, M. A. Thomas, and M. Thommes, "Micropore analysis." *Characterization of Porous Solids and Powders: Surface Area, Pore Size and Density*, ed. S. Lowell et al. (Dordrecht)(Springer Netherlands) p. 129 (2004).
27. S. Kabir, D. J. Myers, N. Kariuki, J. Park, G. Wang, A. Baker, N. Macauley, R. Mukundan, K. L. More, and K. C. Neyerlin, "Elucidating the dynamic nature of fuel cell electrodes as a function of conditioning: an ex situ material characterization and in situ electrochemical diagnostic study." *ACS Appl. Mater. Interfaces*, **11**, 45016 (2019).
28. S. Stariha, N. Macauley, B. T. Sneed, D. Langlois, K. L. More, R. Mukundan, and R. L. Borup, "Recent advances in catalyst accelerated stress tests for polymer electrolyte membrane fuel cells." *J. Electrochem. Soc.*, **165**, F492 (2018).
29. R. Makharia, M. Mathias, and D. Baker, "Measurement of catalyst layer electrolyte resistance in PEFCs using electrochemical impedance spectroscopy." *J. Electrochem. Soc.*, **152**, A970 (2005).
30. D. R. Baker, D. A. Caulk, K. C. Neyerlin, and M. W. Murphy, "Measurement of oxygen transport resistance in PEM fuel cells by limiting current methods." *J. Electrochem. Soc.*, **156**, B991 (2009).
31. M. J. Dzara, A. O. Godoy, M. Odgaard, B. Zulevi, A. Serov, J. Jankovic, and S. Pylypenko, "Physicochemical Properties of ECS Supports and Pt/ECS Catalysts." *ACS Appl. Energy Mater.*, **4**, 9111 (2021).
32. S. H. Joo, S. J. Choi, I. Oh, J. Kwak, Z. Liu, O. Terasaki, and R. Ryoo, "Ordered nanoporous arrays of carbon supporting high dispersions of platinum nanoparticles." *Nature*, **412**, 169 (2001).
33. V. Yarlagadda, N. Ramaswamy, R. S. Kukreja, and S. Kumaraguru, "Ordered mesoporous carbon supported fuel cell cathode catalyst for improved oxygen transport." *J. Power Sources*, **532**, 231349 (2022).
34. K. Shinozaki, H. Yamada, and Y. Morimoto, "Relative humidity dependence of Pt utilization in polymer electrolyte fuel cell electrodes: effects of electrode thickness,

ionomer-to-carbon ratio, ionomer equivalent weight, and carbon support." *J. Electrochem. Soc.*, **158**, B467 (2011).
35. T. Kaneko, J. Ooyama, M. Ohki, H. Kanesaka, Y. Yoshimoto, and I. Kinefuchi, "Effect of ionomer swelling and capillary condensation of water on porous characteristics in cathode catalyst layers of polymer electrolyte membrane fuel cells under humidified conditions." *Int. J. Heat Mass Transfer*, **200**, 123491 (2023).
36. K. Karan, "PEFC catalyst layer: recent advances in materials, microstructural characterization, and modeling." *Curr. Opin Electrochem.*, **5**, 27 (2017).
37. L. Hu, T. Van Cleve, H. Yu, J. H. Park, N. Kariuki, A. J. Kropf, R. Mukundan, D. A. Cullen, D. J. Myers, and K. C. Neyerlin, "Electrochemical characterization of evolving ionomer/electrocatalyst interactions throughout accelerated stress tests." *J. Power Sources*, **556**, 232490 (2023).
38. S.-M. Lee, S.-H. Lee, and J.-S. Roh, "Analysis of activation process of carbon black based on structural parameters obtained by XRD analysis." *Crystals*, **11**, 153 (2021).
39. Y.-C. Park, H. Tokiwa, K. Kakinuma, M. Watanabe, and M. Uchida, "Effects of carbon supports on Pt distribution, ionomer coverage and cathode performance for polymer electrolyte fuel cells." *J. Power Sources*, **315**, 179 (2016).
40. J. R. Gallagher et al., "In situ diffraction of highly dispersed supported platinum nanoparticles." *Catal. Sci. Technol.*, **4**, 3053 (2014).
41. H. G. T. Nguyen et al., "Reference isotherms for water vapor sorption on nanoporous carbon: results of an interlaboratory study." *Adsorption*, **29**, 113 (2023).
42. W. Gu, D. R. Baker, Y. Liu, and H. A. Gasteiger, "Proton exchange membrane fuel cell (PEMFC) down-the-channel performance model." *Handbook of Fuel Cells, Fundamentals Technology and Applications* (Hoboken, NJ)(John Wiley & Sons, Ltd.) (2010).
43. R. K. F. Della Bella, B. M. Stühmeier, and H. A. Gasteiger, "Universal correlation between cathode roughness factor and H2/air performance losses in voltage cycling-based accelerated stress tests." *J. Electrochem. Soc.*, **169**, 044528 (2022).
44. R. Kou et al., "Stabilization of electrocatalytic metal nanoparticles at metal-metal oxide-graphene triple junction points.." *J. Am. Chem. Soc.*, **133**, 2541 (2011).